

REPORT DOCUMENTATION PAGE				<i>Form Approved</i> <i>OMB No. 0704-0188</i>	
<small>Public reporting burden for this collection of information is estimated to average 1 hour per response, including the time for reviewing instructions, searching existing data sources, gathering and maintaining the data needed, and completing and reviewing this collection of information. Send comments regarding this burden estimate or any other aspect of this collection of information, including suggestions for reducing this burden to Department of Defense, Washington Headquarters Services, Directorate for Information Operations and Reports (0704-0188), 1215 Jefferson Davis Highway, Suite 1204, Arlington, VA 22202-4302. Respondents should be aware that notwithstanding any other provision of law, no person shall be subject to any penalty for failing to comply with a collection of information if it does not display a currently valid OMB control number. PLEASE DO NOT RETURN YOUR FORM TO THE ABOVE ADDRESS.</small>					
1. REPORT DATE (DD-MM-YYYY)		2. REPORT TYPE		3. DATES COVERED (From - To)	
4. TITLE AND SUBTITLE				5a. CONTRACT NUMBER	
				5b. GRANT NUMBER	
				5c. PROGRAM ELEMENT NUMBER	
6. AUTHOR(S)				5d. PROJECT NUMBER	
				5e. TASK NUMBER	
				5f. WORK UNIT NUMBER	
7. PERFORMING ORGANIZATION NAME(S) AND ADDRESS(ES)				8. PERFORMING ORGANIZATION REPORT NUMBER	
9. SPONSORING / MONITORING AGENCY NAME(S) AND ADDRESS(ES)				10. SPONSOR/MONITOR'S ACRONYM(S)	
				11. SPONSOR/MONITOR'S REPORT NUMBER(S)	
12. DISTRIBUTION / AVAILABILITY STATEMENT					
13. SUPPLEMENTARY NOTES					
14. ABSTRACT					
15. SUBJECT TERMS					
16. SECURITY CLASSIFICATION OF:			17. LIMITATION OF ABSTRACT	18. NUMBER OF PAGES	19a. NAME OF RESPONSIBLE PERSON
a. REPORT	b. ABSTRACT	c. THIS PAGE			19b. TELEPHONE NUMBER (include area code)

Ocean Surface Wave Optical Roughness – Analysis of Innovative Measurements

Michael L. Banner

School of Mathematics and Statistics, The University of New South Wales, Sydney 2052,
Australia

Tel: (+61-2) 9385-7071 fax: (+61-2) 9385-7123 email: m.banner@unsw.edu.au

Russel P. Morison

School of Mathematics and Statistics, The University of New South Wales, Sydney 2052,
Australia

Tel: (+61-2) 9385-7064 fax: (+61-2) 9385-7123 email: r.morison@unsw.edu.au

Award #: N00014-11-1-0054

LONG-TERM GOALS

We are part of a multi-institutional research team funded by the ONR-sponsored Radiance in a Dynamic Ocean (RaDyO) program. The primary research goals of the program are to (1) examine time-dependent oceanic radiance distribution in relation to dynamic surface boundary layer (SBL) processes; (2) construct a radiance-based SBL model; (3) validate the model with field observations; and (4) investigate the feasibility of inverting the model to yield SBL conditions. Our goals are to contribute innovative measurements, analyses and models of the sea surface roughness at length scales as small as a millimeter. This characterization includes microscale and whitecap breaking waves.

The members of the research team are

Michael Banner, School of Mathematics, UNSW, Sydney, Australia

Johannes Gemmrich, Physics and Astronomy, UVic, Victoria, Canada

Russel Morison, School of Mathematics, UNSW, Sydney, Australia

Howard Schultz, Computer Vision Laboratory, Computer Science Dept, U. Mass., Mass

Christopher Zappa, Lamont Doherty Earth Observatory, Palisades, NY

OBJECTIVES

Nonlinear interfacial roughness elements - sharp crested waves, breaking waves as well as the foam, subsurface bubbles and spray they produce, contribute substantially to the distortion of the optical transmission through the air-sea interface. These common surface roughness features occur on a wide range of length scales, from the dominant sea state down to capillary waves. Wave breaking signatures range from large whitecaps with their residual passive foam, down to the ubiquitous centimetre-scale microscale breakers that do not entrain air. There is substantial complexity in the local wind-driven sea surface roughness microstructure, including very steep

nonlinear wavelets and breakers. Traditional descriptors of sea surface roughness are scale-integrated statistical properties, such as significant wave height, mean squared slope [e.g., *Cox and Munk*, 1954a] and breaking probability [e.g., *Holthuijsen and Herbers*, 1986]. Subsequently, spectral characterisations of wave height, slope and curvature have been measured, providing a scale resolution into Fourier modes for these geometrical sea roughness parameters. More recently, measurements of whitecap crest length spectral density [e.g., *Gemmrich et al.*, 2008; *Phillips et al.*, 2001] and microscale breaker crest length spectral density [e.g., *Jessup and Phadnis*, 2005] have been reported.

Our effort seeks to provide a more comprehensive description of the physical and optical roughness of the sea surface. We will achieve this through the analysis of our suite of comprehensive sea surface roughness observational measurements within the RADYO field program. These measurements are designed to provide optimal coverage of fundamental optical distortion processes associated with the air-sea interface. In our data analysis, and complementary collaborative effort with RaDyO modelers, we are investigating both spectral and phase-resolved perspectives. These will allow refining the representation of surface wave distortion in present air-sea interfacial optical transmission models.

APPROACH

We build substantially on our accumulated expertise in sea surface processes and air-sea interaction. We are working within the larger team (listed above) measuring and characterizing the surface roughness. This team is contributing the following components to the primary sea surface roughness data gathering effort in RaDyO:

- polarization camera measurements of the sea surface slope topography, down to capillary wave scales, of an approximately 1m x 1m patch of the sea surface (see Figure 1), captured at video rates. [Schultz, Zappa]
- co-located and synchronous orthogonal 75 Hz linear scanning laser altimeter data to provide spatio-temporal properties of the wave height field (resolved to $O(0.5\text{m})$ wavelengths) [Banner, Morison]
- high resolution video imagery to record whitecap data from two cameras, close range and broad field [Gemmrich]
- fast response, infrared imagery to quantify properties of the microscale breakers, and surface layer kinematics and vorticity [Zappa]
- air-sea flux package including sonic anemometer to characterize the near-surface wind speed and wind stress [Zappa]

The team's envisaged data analysis effort includes: detailed analyses of the slope field topography, including mean square slope, skewness and kurtosis; laser altimeter wave height and large scale wave slope data; statistical distributions of whitecap crest length density in different scale bands of propagation speed and similarly for the microscale breakers, as functions of the wind speed/stress and the underlying dominant sea state. Our contributions to the modeling effort will focus on using RaDyO data to refine the sea surface roughness transfer function. This includes the representation of nonlinearity and breaking surface wave effects including bubbles, passive foam, active whitecap cover and spray, as well as micro-breakers.

WORK COMPLETED

Our effort in FY12 comprised further analysis of the suite of atmospheric fluxes and sea surface roughness measurements gathered from FLIP during the RaDyO field experiments in the Santa Barbara channel during September 5-27, 2008 and Hawaii during August 23-September 16, 2009. We participated actively in refining the analysis and validation of the polarimetric and wave breaking data. We also carried out further processing, validation and archiving of our scanning lidar data collocated with our partner investigators' high resolution polarimetric, infrared and optical imaging. This data provides the large-scale wave geometry (height and slope) throughout the observational periods.

Our effort in FY13 comprised further collaborative analysis of the sea surface roughness measurements gathered from FLIP during the RaDyO field experiments in the Santa Barbara channel during Sept. 5-27, 2008 and Hawaii during Aug. 23-Sept. v16, 2009. We participated actively in extending our analysis and validation of the polarimetric and wave breaking data. We submitted two publications. One is in press [*Gemmrich et al.*, 2013] and one is in revision [*Banner et al.*, 2013].

RESULTS

To provide the context of our new results for FY13, during the SBC experiment, diurnal processes were the origin of most of the variability in the atmospheric and oceanic forcing. The momentum, sensible heat and latent heat fluxes all show a diurnal cycle similar to the wind speed. In strong contrast, in the HI experiment, processes were driven by the persistent easterly trade winds. This overview of the background air-sea flux conditions was obtained from time series of momentum (wind stress), sensible heat, and water vapor direct covariance fluxes during the Santa Barbara Channel (hereafter SBC) and central Pacific Ocean studies of Hawaii (hereafter HI). Full details are provided in *Zappa et al.* [2012] and *Dickey et al.* [2012].

TOGA-COARE and Air-sea fluxes

Time series of momentum (wind stress), sensible heat, and water vapor direct covariance fluxes during the Santa Barbara Channel study are shown in the left panel of Figure 1. Also shown are the TOGA-COARE model bulk fluxes [*Fairall et al.*, 2003]. Diurnal processes were the origin of most of the variability in the atmospheric and oceanic forcing. The momentum, sensible heat and latent heat fluxes all show a diurnal cycle similar to the wind speed. Time series of momentum (wind stress), sensible heat, and water vapor direct covariance fluxes during the central Pacific Ocean study south of Hawaii are shown in the right panel of Figure 1. Here, processes were driven by the persistent easterly trade winds.

The RaDyO flux data tracks the TOGA-COARE 3.0 model prediction closely. The measured sensible heat flux is within 1.1 W m^{-2} of the TOGA-COARE 3.0 model prediction for SBC and within 2.1 W m^{-2} for the Pacific Ocean south of Hawaii. The TOGA-COARE 3.0 model prediction overestimates the measured latent heat flux by at most 31.6 % for SBC and 21.8 % for the Pacific Ocean south of Hawaii. *Edson* [2008] has observed similar tendencies of this magnitude in his extensive datasets including CLIVAR MOde Water Dynamic Experiment

(CLIMODE), Coupled Boundary Layer and Air-Sea Transfer (CBLAST) Experiment, Marine Boundary Layer (MBL) Experiment, and Risø Air-Sea Experiment (RASEX). Edson is incorporating these observations into the latest TOGA-COARE 4.0 model transfer coefficients where the Dalton number needs to be reduced by up to 25% for winds below 10 m s^{-1} (see Figure 8 in *Edson [2008]*). Thus, the greater overestimation observed in SBC for the latent heat flux is consistent with the larger corrections at lower wind speeds proposed by *Edson [2008]*. Our observations during the RaDyO experiments in SBC and in the Pacific Ocean south of Hawaii provide independent validation of these effects.

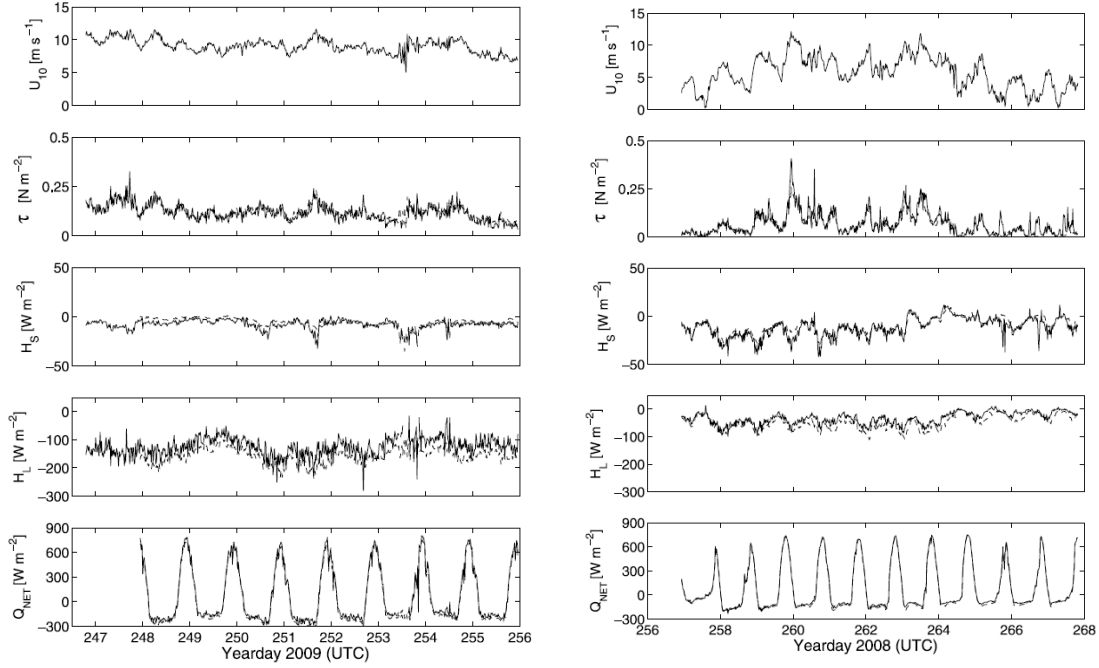


Figure 1. Time series of wind speed U_{10} , momentum flux (wind stress) τ , sensible heat flux H_s , latent heat flux H_l , and net heat flux Q_{net} during the Santa Barbara Channel experiment (left panel) and during the central Pacific Ocean experiment south of Hawaii (right panel). Solid lines use direct covariance measurements and dashed lines use TOGA-COARE bulk fluxes.

We note that the dynamic range of the wind stress is larger during the SBC experiment than the Hawaii experiment. Together these two experiments provide an interesting variety of sea state conditions including light and variable to strongly white-capping. They provide a valuable test bed for mean square slope and breaking measurements over an interesting dynamic range of wind speeds.

Short ocean wave microstructure

Historically, measuring the full two-dimensional, time-varying structure of millimeter scale waves in the open ocean has proven difficult. The major shortcomings of the most remote sensing and in-situ methods have been the inability to extract sufficient information about the full two-dimensional slope field and to construct an instrument that does not disturb the air-sea

interface. Figure 2 (TOP) shows sample x- and y-slope images from the Narrow field-of-view Imaging Polarimeter (N-IPol) instrumentation. We captured time-lapsed video at 60 Hz of the X and Y Slope images. A map of the local wave height topography of the imaged patch of the sea surface that is riding on the larger-scale dominant wave is found by integrating the two-dimensional slope field using the method outlined by Frankot and Chellappa [1988] and is shown in Figure 2 (BOTTOM). These slope features are characterized by steep slopes that also have high spatial variance that exhibits a dimpled structure observed previously in the laboratory by Zappa *et al.* [2004]. The N-IPOL has provided useful data on the local directional slope of the gravity waves, and the 1-meter baseline slope intercomparison with the LIDAR slope shows a high (0.8) magnitude squared coherence level. In addition, the polarimeter data characterizes the background environment experienced by the very short wind waves that comprise the sea surface microstructure. These short wave spectra capture data at comparable scales as previously in Hara *et al.* [1998], but without any instrument disturbances to the sea surface. This information allows accurate phasing of the polarimetric camera imagery of the sea surface microstructure with respect to the underlying dominant wind waves. For instance, a new polarimetric imaging camera highlights the complex interplay of processes in shaping the roughness of the sea surface. These small-scale slope observations by polarimetry highlight the possible oversimplification of the classic Cox-Munk view that mss increases linearly with wind speed (see Figure 3). They

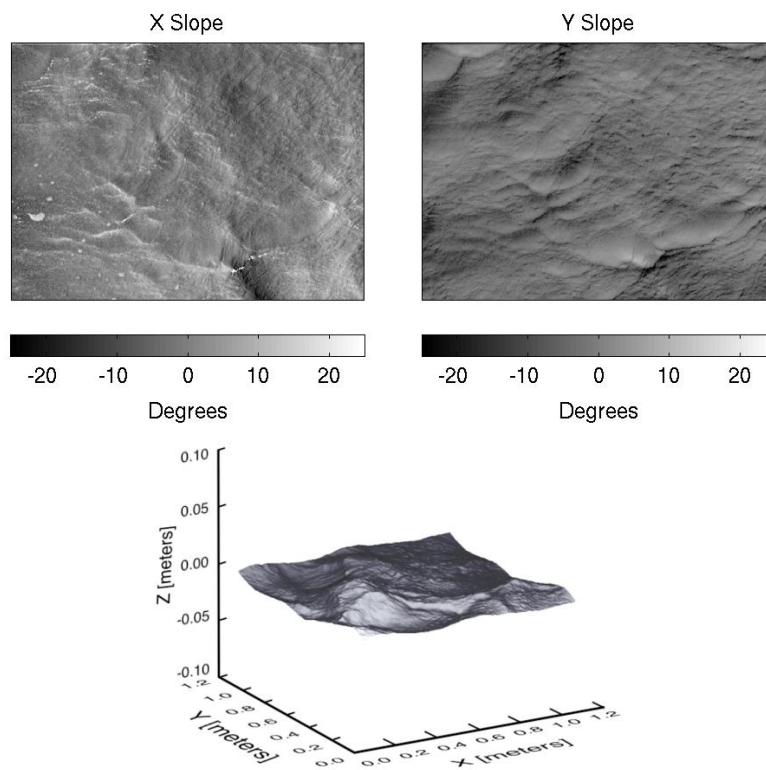


Figure 2. (TOP) A typical gray-scale image of the X- (Left) and Y-Slope (Right) slope field of a small patch of sea surface roughly 1 m by 1m during the Santa Barbara Channel experiment with a wind speed of 9.2 m s^{-1} . (BOTTOM) Representative frame from a video sequence showing a reconstructed wave train for the same data shown in TOP. The spatial resolution is 1.5mm and the temporal resolution is 60Hz.

suggest the potential importance of upper-ocean currents in addition to the wind. In the wind direction, wave energy follows the deep water dispersion relationship at wave numbers at least up to 100 rad m^{-1} and apparent frequencies up to 40 rad s^{-1} . At higher wave numbers and frequencies the wave energy spreads but does not depart from the mean dispersion curve for zero-mean current. As the wavelength increases, the wind drift influence on propagation decreases, typically vanishing for wavelengths greater than $O(1 \text{ m})$ at moderate wind speeds. The wavenumber-frequency spectrum in the cross-wind direction shows a systematic deviation from the mean dispersion curve for zero-mean current. It is seen that for wave numbers at least up to 100 rad m^{-1} , the slope energy conforms to this Doppler modified dispersion relationship. These results are timely considering issues raised in the recent review article on the conundrums of capillary-gravity waves [Munk, 2009].

Our results are compared with the classical Cox-Munk results [Cox and Munk, 1954a; b] in Figure 4 as well as our more recent laboratory and field measurements using scanning laser slope gauges. We observe the MSS to increase with wind speed, but not linearly as observed by the classic Cox-Munk relationship. We observe more variability than reported by Cox-Munk.

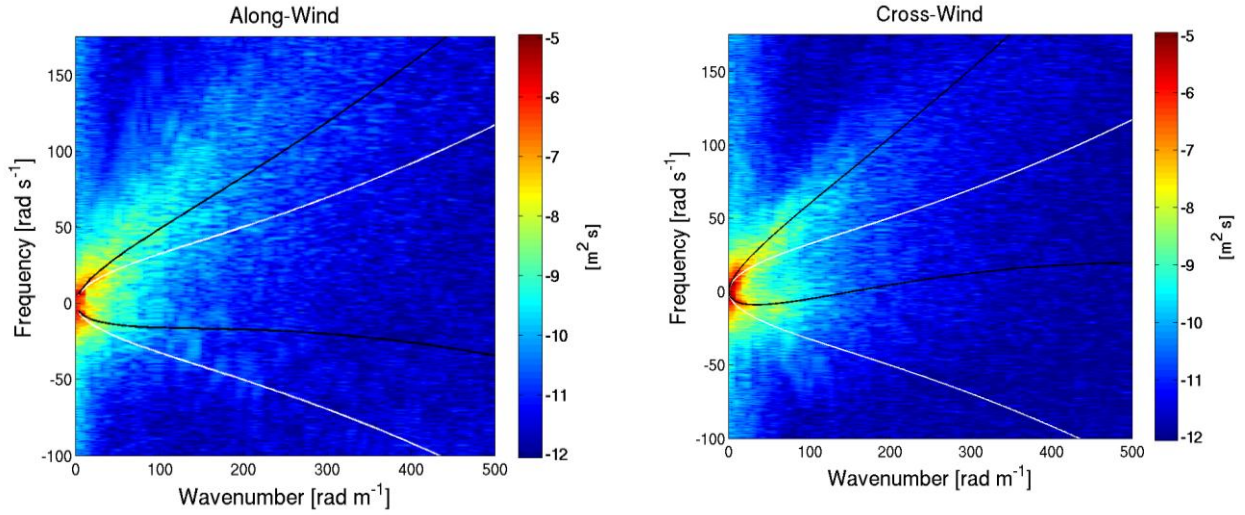


Figure 3. Wavenumber-frequency spectrum from the polarimeter data in the wind (left) and cross-wind (right) directions during the RaDyO Santa Barbara Channel Experiment with a wind speed of 5.5 m s^{-1} and an upper-ocean current speed U_c of 27.3 cm s^{-1} with a relative direction to the wind of 110° . Here, the wind direction and current direction both follow the oceanographic convention of "towards". Positive frequencies are representative of waves propagating in the direction of the forcing. The white trace in each plot is the deep-water dispersion relationship for ocean waves. The black trace in each plot shows that a given wavenumber vector, \vec{k} , is Doppler shifted from its intrinsic frequency, ω_o , to its observed mean frequency, ω , by $U_c \cdot \vec{k}$, where U_c is the net surface transport velocity for waves of scale \vec{k} . In the absence of along-wind ocean currents, U_c is the wind-drift velocity. U_c is the measured cross-wind ocean current.

Within our measured variability there exist noted trends as highlighted by the red, green blue circles (discussed below). Note that the Santa Barbara Experiment results compare well with the Cox-Munk relationships for slick conditions which are consistent with the surfactant levels in the region during the experiment. Publication of the first manuscript demonstrating the feasibility of the polarimetric slope sensing technique was completed. The manuscript was published in Measurement, Science and Technology entitled “Retrieval of short ocean wave slope using polarimetric imaging” [Zappa *et al.*, 2008].

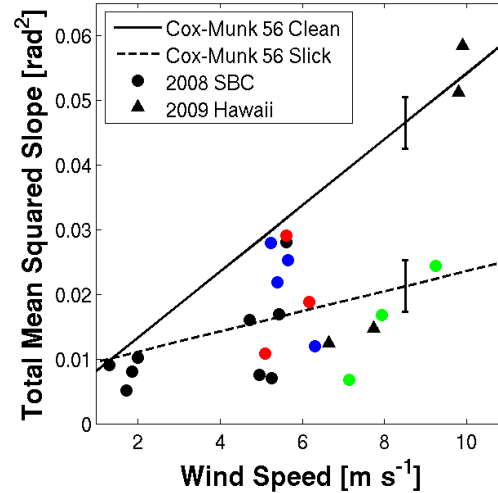


Figure 4. Mean squared total slope against wind speed during the Santa Barbara Channel and Hawaii RaDyO field experiments. The red symbols represent Episode I, the blue symbols represent Episode II, green symbols represent Episode III, and the black symbols represent the rest of the polarimeter data. The solid and dashed lines represent the Cox and Munk [1956] best linear fits to their clean surface and slick-covered surface results. Error bounds on Cox and Munk [1956] best linear fits shown are \pm one standard deviation.

Three Episodes of Local Trends in MSS

The data does not always conform to the linear Cox-Munk relationship of MSS to wind speed, and at times has shown a reversal of the Cox-Munk linear relationship. Furthermore, we observe measurable changes in the directional spectra showing distortion of the short-wave patterns by the currents. This phenomenon has been demonstrated in the wavenumber-frequency spectra examples in Figure 3. In Episode I, the MSS doubles even though the wind speed increases only slightly from 4.6 to 6.5 m s^{-1} and the dominant wind sea does not change. We attribute the increase in mss primarily to the response of the small-scale gravity-capillary waves to the increase in wind speed. Wind speed sensitivity of the spectrum increases toward smaller scales. This underpins the principles of Bragg scatterometry. In Episode II, the MSS halved even though the wind speed increases from 5.2 to 7.1 m s^{-1} . The dominant wind sea decreased and the spectral level is nearly halved over the range of 0.1 to 3.0 Hz. Here, the MSS is less sensitive to smaller scales. In Episode III, the MSS halves and the wind speed decreases from 9.5 to 7.3 m s^{-1} . The dominant wind sea downshifted from 0.25 to 0.20 Hz with an increase of 10% in wave energy. The currents are noted to increase from 6.4 to 20.5 cm s^{-1} with a direction that is roughly 0° to 20° relative to the wind. The omni-directional wave number slope spectra

show the decrease in slope spectral energy was dominated by scales between 7 and 300 rad m^{-1} . Even though a modest increase in the dominant wind sea energy occurs, we attribute the decrease in mss primarily to the response of the small-scale gravity-capillary waves to the decrease in wind speed and the increasing current approximately in the direction of the wind. Co-flowing wind and current tends to reduce the input forcing to the waves, especially for the slower-moving short components, and consequently a reduction in their slope.

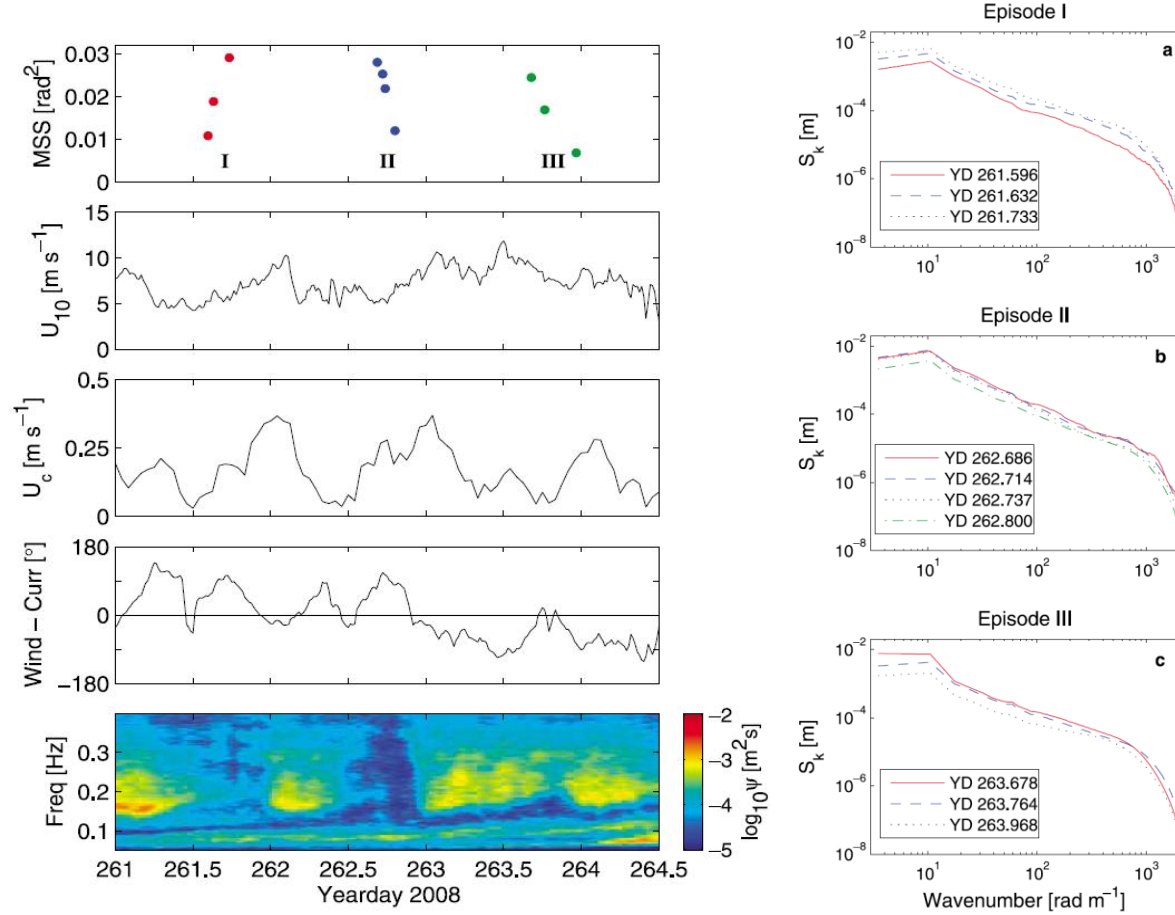


Figure 5. (LEFT) Time series of the total mean square slope (mss), wind speed, ocean current speed, wind direction relative to the current direction, and the wave height spectrogram for a subset of the Santa Barbara Channel experiment. Here the wind direction and current direction both follow the oceanographic convention of “toward.” The color code identifying episodes I, II, and III is the same as in Figure 4. (RIGHT) Omnidirectional wave number spectra for (a) episode I, (b) episode II, and (c) episode III shown on LEFT. The yearday is indicated to highlight the progression of runs within an episode.

Incorporating Surface Roughness Measurements into Modeling

Nonlinear interfacial roughness elements - sharp crested waves, breaking waves as well as the foam, subsurface bubbles and spray they produce, contribute substantially to the distortion of the optical transmission through the air-sea interface. The passage of open ocean whitecaps at

different scales shades the subsurface light field transiently. Microbreaking will modulate the refraction of light at the air-sea interface and will contribute minimally to the shading. We have collaborated with **George Kattawar and Yu You** to provide the wave slope data from the N-IPol camera to replace their synthetic wave slope spectra in their simulations [You *et al.*, 2011]. We are also collaborating with **Marlon Lewis** to examine the relevant time-dependent geometrical properties of the surface wave and roughness characteristics as well as the breaking wave front and trailing foam patches including their spatial and temporal scales. Wei *et al.* [2013] have shown that surface waves have characteristic imprints in irradiance profiles. Specifically, larger waves (with longer wavelengths) are dominant contributors to fluctuations at deeper depths while smaller waves (with shorter wavelengths) are more important in shallower regions in the water column. We examine the effect of wave breaking events on the radiation distribution detected by a subsurface camera (RadCam) at varying depths directly beneath the surface imagery. This effort will provide a far more detailed characterization of the wind driven air-sea interface, including wave breaking (whitecaps and microscale breaking). This is needed to provide more complete parameterizations of these processes, which will improve the accuracy of ocean optical radiative transfer models and trans-interfacial image reconstruction techniques.

Breaking crest length distributions

In response to the growing need for robust validation data for the *Phillips* [1985] breaking wave spectral framework, we contribute new field results observed from R/P FLIP for the breaking crest length distributions during two different wind-wave conditions, and breaking strength during one wind-wave condition. According to *Phillips* [1985], the scale of each breaking front wave is associated with the phase speed of the underlying wave that is breaking, and the associated width of the breaking front contributes at that scale to the distribution of mean breaking crest width/unit sea surface area, $\Lambda(c)$. Here we characterize each breaking front velocity by its initial observed velocity c_b , where $c_b = \alpha c$, where $\alpha \sim 0.8$, and define the azimuthally-integrated crest length distribution of measured $\Lambda(c_b)$. Then, according to *Phillips* [1985] breaking wave spectral framework, the spectral distribution of wave energy dissipation rate $\varepsilon(c_b)$ is given by $\varepsilon(c_b) = b(c_b) \rho g^{-1} c_b^{-5} \Lambda(c_b)$, where $b(c_b)$ is the scale dependent breaking strength coefficient that links the breaker front kinematics to the energetics and dynamics of the breaking waves. The water density is ρ and g is the gravitational acceleration.

The first experiment in the SBC had developing seas and the second experiment near HI had mature seas. These are amongst the first experiments to use dissipation rate measurements probing up into the breaking crest together with simultaneous measurements of breaking crest length distributions. Of particular interest is that the dynamic range of the wind stress is larger during the SBC experiment than the Hawaii experiment. Together these two experiments provide wave breaking measurements over an interesting dynamic range of wind speeds spanning light and variable to strong.

Results on the breaking crest length distribution $\Lambda(c_b)$ for the two experiments are given in Fig. 6. A key feature of all observed $\Lambda(c_b)$ distributions at both experimental sites is a maximum at short-to-intermediate wave scales. The location of this maximum, which specifies the scale of the largest contribution of breaking crests, increases with wave age, however there is no clear

dependence on wave age of the magnitude of this maximum. Wind speed and wave field parameters covered a much broader range during the Santa Barbara Channel experiment compared to the experiment in the central Pacific Ocean south of Hawaii. These differences in the dynamic range of forcing parameters are directly reflected in the dynamic range of the breaking crest length distributions. At intermediate scales, i.e. $3 \text{ m/s} \leq c_b \leq 5 \text{ m/s}$, the $\Lambda(c_b)$ distributions span almost two orders of magnitude in SBC, but only a factor $O(5)$ in HI. The maximum levels of $\Lambda(c_b)$ are comparable between the two experiments, but the overall mean level of $\Lambda(c_b)$ is larger in HI. It is seen that the slope of the $\Lambda(c_b)$ curves for higher c_b values fluctuates about the *Phillips* [1985] canonical form $\Lambda(c_b) \sim c_b^{-6}$, which is discussed further below.

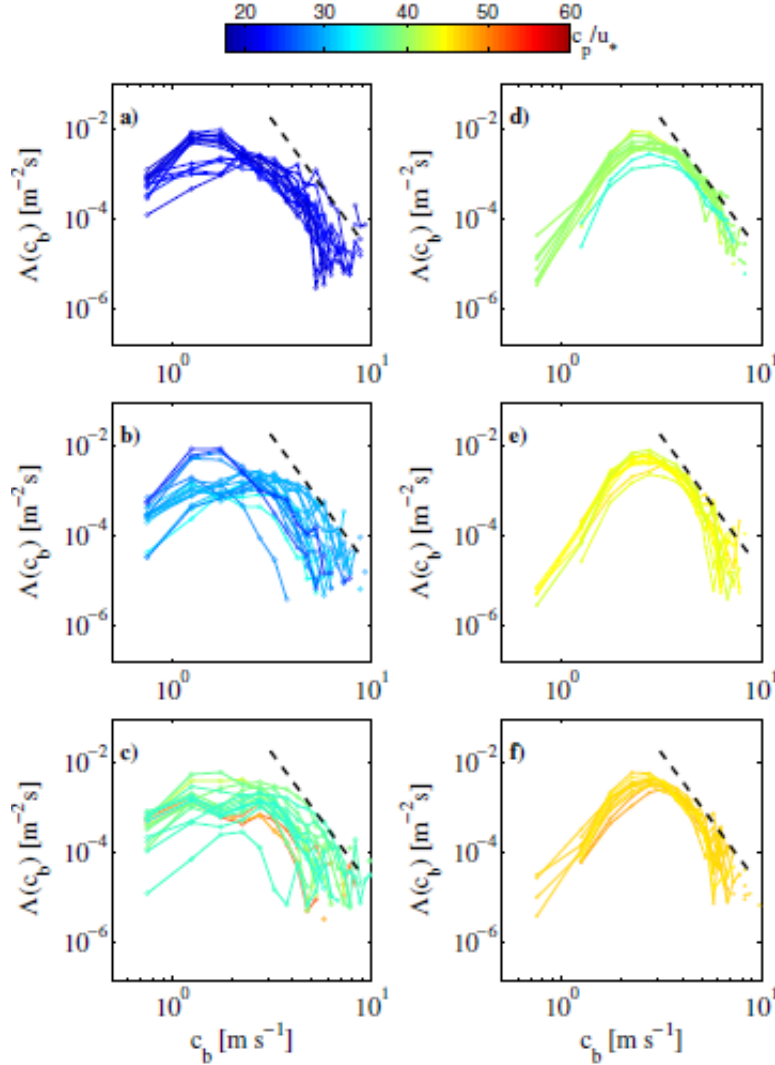


Figure 6. Distributions of spectral breaking crest length per unit area, $\Lambda(c_b)$, against observed breaker speed c_b during the experiments in Santa Barbara Channel (a-c) and Hawaii (d-f). Colors represent wave age c_p/u_* . The dashed line indicates the $m = -6$ slope predicted by *Phillips* [1985]. For each experiment, data runs are split into 3 equal-sized sub-panels, covering the wave age sub-ranges during the entire data sets.

There are some noteworthy differences in the shape of breaking crest length distributions of the two data sets, likely associated with different development stages of the wave field. We calculated overall mean distributions from 24 SBC runs with $c_p/u_* \leq 25$, characterizing growing seas, and from 14 HI runs with $c_p/u_* \geq 45$, characterizing mature seas. These are shown in the left panel of Fig.3. There were no comparably mature sea states from the SBC data set to include. In growing seas, breaking spans the entire spectrum from dominant waves to scales associated with $0.1c_p$, where c_p is the speed of the spectral peak waves, whereas in mature seas no breaking is observed at scales larger than those corresponding to $0.6c_p$.

The normalized fifth moment of the breaking crest length distributions is shown in the right panel of Fig. 7. The fifth moment of the $\Lambda(c_b)$ distribution is related to the spectral energy dissipation rate. The strongest dissipation rate is seen to occur at small-to-intermediate scales in the mature sea, but at the large wave scale in the developing sea. Thus the velocity scale of the peak of the breaking dissipation rate decreases with increasing wave age. Despite the breaking in mature seas occurring over a smaller spectral bandwidth than in growing seas, the total dissipation rate in the mature seas is about three times higher. This is attributed to higher energy and momentum fluxes from the wind in HI.

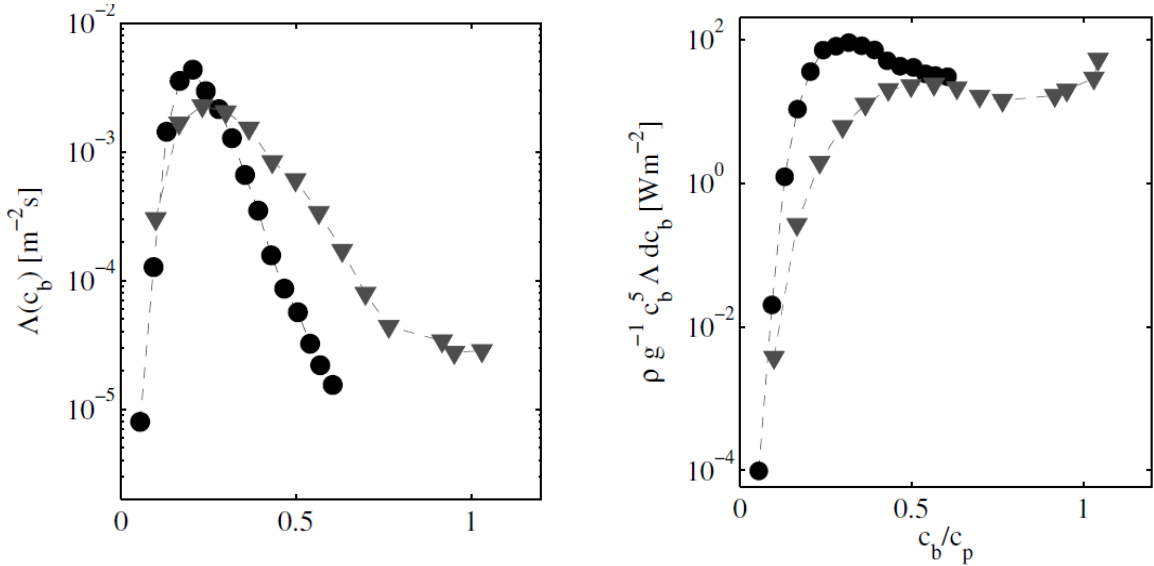


Figure 7. Overall mean breaking crest length distributions (left panel) and their 5th moment (right panel), for subsets of the data representing developing seas (gray triangles) and mature seas (black circles).

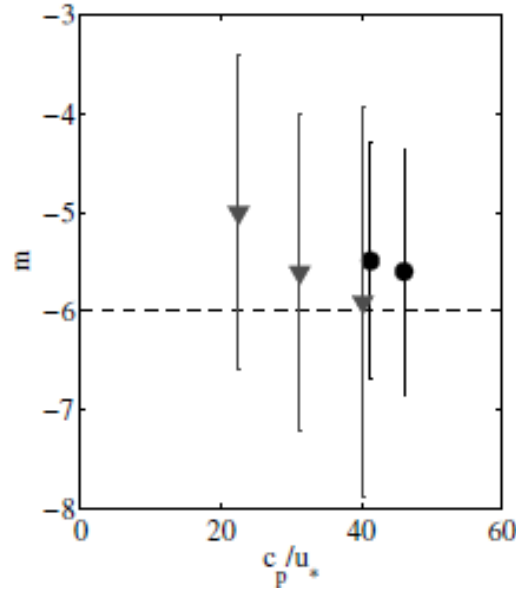


Figure 8. Bin-averaged exponent m (slope) of the breaking crest length distribution as function of wave age (c_p/u_*) for the Santa Barbara channel (gray triangles) and Hawaii experiment (black circles). The dashed line depicts the classical Phillips [1985] result $m=-6$. The vertical bars indicate ± 1 standard deviation.

Further, in Fig. 8, it is seen that the breaking crest length spectrum tends to fall off more slowly than the c^{-6} behavior predicted by Phillips [1985]. This result was statistically significant at the 95% confidence level. We note that this conclusion is weakly sensitive to the data processing methodology used, as discussed below.

Breaking strength parameter b

We note that the transition from the kinematic quantity of the crest length distribution to the dynamics of energy dissipation rate requires knowledge of the breaking strength parameter b . Estimates of the spectrally-resolved breaking parameter are only starting to become available and all previous studies based on field data report the scale-integrated value b_{eff} . Reported values of b_{eff} from different experiments span more than 3 orders of magnitude between these experiments, from 3×10^{-5} to 7×10^{-2} [Gemrich *et al.*, 2008; Melville and Matusov, 2002; Thomson *et al.*, 2009]. From our direct measurements of $\Lambda(c_b)$ and surface-piercing dissipation rates in the mature wind seas off HI, we directly measured the effective breaking strength parameter b_{eff} to be $4.2 \pm 1.8 \times 10^{-5}$ for the wave age (c_p/u_*) range of 40-47.

Sensitivity to data analysis methodology

In view of the rather large scatter in b_{eff} reported by different investigators pointed out above, we revisited the sensitivity of the whitecap analysis methodology. While there are differences in the detailed measurement of the individual breaker geometry, a significant source of variation arises because some investigators have chosen to partition the time-dependent geometry of each

breaker into variable speed bins as the breaker slows down, while other investigators, including ourselves, assign the mean crest length of a given breaker to its initial speed, as envisaged by Phillips [1985]. The variable speed allocation method has the effect of aliasing $\Lambda(c_b)$ to slower waves, thereby increasing the exponent $-m$. Our analysis based on the RaDyO data sets estimates this difference in the exponent to be close to 1. The corresponding impact on b_{eff} for the RaDyO data was a factor of $O(2)$ increase associated with the variable-speed method. We are investigating other possible sources that may be contributing to the large dynamic range of reported b_{eff} values.

IMPACT/APPLICATIONS

This effort contributes a more detailed characterization of the wind driven air-sea interface, including wave breaking (whitecaps and microscale breaking). This is needed to provide more complete parameterizations of these processes, which will improve the accuracy of ocean optical radiative transfer models and trans-interfacial image reconstruction techniques.

REFERENCES

- Banner, M. L., C. J. Zappa and J. Gemmrich (2013), A note on Phillips' spectral framework for ocean whitecaps, *Journal of Physical Oceanography*, in revision.
- Cox, C., and W. Munk (1954a), Measurement of the roughness of the sea surface from photographs of the sun's glitter, *Journal of the Optical Society of America*, 44(11), 838-850.
- Cox, C., and W. Munk (1954b), Statistics of the sea surface derived from sun glitter, *Journal of Marine Research*, 13(2), 198-227.
- Cox, C., and W. Munk (1956), Slopes of the sea surface deduced from photographs of sun glitter, *Bulletin of the Scripps Institution of Oceanography*, 6(9), 401-487.
- Dickey, T., et al. (2012), Introduction to special section on recent advances in the study of optical variability in the near-surface and upper ocean, *Journal of Geophysical Research – Oceans*, 117(C00H20), doi:10.1029/2012JC007964.
- Edson, J. B. (2008), Review of Air-Sea Transfer Processes, in *ECMWF Workshop on Ocean-Atmosphere Interactions*, edited, pp. 7-25, European Centre for Medium Range Forecasts, Reading, UK.
- Fairall, C. W., E. F. Bradley, J. E. Hare, A. A. Grachev, and J. B. Edson (2003), Bulk parameterization of air-sea fluxes: Updates and verification for the COARE algorithm, *J. Climate*, 16, 571-591.
- Gemmrich, J. R., M. L. Banner, and C. Garrett (2008), Spectrally resolved energy dissipation and momentum flux of breaking waves, *J. Phys. Oceanogr.*, 38, 1296-1312.
- Gemmrich, J. R., C. J. Zappa, M. L. Banner, and R. P. Morison (2013), Wave breaking in developing and mature seas, *Journal of Geophysical Research - Oceans*, 118, doi:10.1002/jgrc.20334.
- Hara, T., E. J. Bock, J. B. Edson, and W. R. McGillis (1998), Observation of short wind waves in coastal waters, *Journal of Physical Oceanography*, 28(7), 1425-1438.
- Holthuijsen, L. H., and T. H. C. Herbers (1986), Statistics of breaking waves observed as whitecaps in the open sea, *Journal of Physical Oceanography*, 16, 290-297.

- Jessup, A. T., and K. R. Phadnis (2005), Measurement of the geometric and kinematic properties of microscale breaking waves from infrared imagery using a PIV algorithm, *Meas. Sci. Technol.*, *16*, 1961-1969.
- Melville, W. K., and P. Matusov (2002), Distribution of breaking waves at the ocean surface, *Nature*, *417*, 58-63.
- Munk, W. (2009), An inconvenient sea truth: Spread, steepness, and skewness of surface slopes, *Annu. Rev. Mar. Sci.*, *1*(doi: 10.1146/annurev.marine.010908.163940), 377–415.
- Phillips, O. M. (1985), Spectral and statistical properties of the equilibrium range in wind-generated gravity waves, *Journal of Fluid Mechanics*, *156*, 505-531.
- Phillips, O. M., F. L. Posner, and J. P. Hanson (2001), High resolution radar measurements of the speed distribution of breaking events in wind-generated ocean waves: surface impulse and wave energy dissipation rates, *J. Phys. Oceanogr.*, *31*, 450–460.
- Thomson, J., J. R. Gemmrich, and A. T. Jessup (2009), Energy dissipation and the spectral distribution of whitecaps, *J. Geophys. Res.*, *35*(L1160).
- Wei, J., M. Lewis, R. V. Dommelen, C. J. Zappa, and M. Twardowski (2013), Wave-induced light field fluctuations in measured irradiance depth profiles, *Journal of Geophys. Res.*, in revision.
- You, Y., G. W. Kattawar, K. J. Voss, P. Bhandari, J. Wei, M. Lewis, C. J. Zappa, and H. Schultz (2011), Polarized light field under dynamic ocean surfaces: Numerical modeling compared with measurements, *Journal of Geophysical Research – Oceans*, *116*(C00H05), doi:10.1029/2011JC007278.
- Zappa, C. J., W. E. Asher, A. T. Jessup, J. Klinke, and S. R. Long (2004), Microbreaking and the enhancement of air-water transfer velocity, *J. Geophys. Res.*, *109*(C08S16), doi:10.1029/2003JC001897.
- Zappa, C. J., M. L. Banner, H. Schultz, A. Corrada-Emmanuel, L. B. Wolff, and J. Yalcin (2008), Retrieval of short ocean wave slope using polarimetric imaging, *Measurement Science and Technology*, *19*(055503), doi:10.1088/0957-0233/1019/1085/055503.
- Zappa, C. J., M. L. Banner, J. R. Gemmrich, H. Schultz, R. P. Morison, D. A. LeBel, and T. Dickey (2012), An overview of sea state conditions and air-sea fluxes during RaDyO, *Journal of Geophysical Research – Oceans*, *117*(C00H19), doi:10.1029/2011JC007336.

PUBLICATIONS

Banner, M. L., C. J. Zappa, and J. Gemmrich (2013), A note on Phillips' spectral framework for ocean whitecaps, *Journal of Physical Oceanography*. [In Revision, Refereed].

Dickey, T., et al. (2012), Introduction to special section on Recent advances in the study of optical variability in the near-surface and upper ocean, *Journal of Geophysical Research – Oceans*, *117*(C00H20), doi:10.1029/2012JC007964. [Published, Refereed].

Gemmrich, J., C. J. Zappa, M. L. Banner, and R. P. Morison (2013), Wave breaking in developing and mature seas, *Journal of Geophysical Research - Oceans*, *118*, doi:10.1002/jgrc.20334. [Published, Refereed].

Zappa, C. J., M. L. Banner, J. R. Gemmrich, H. Schultz, R. P. Morison, D. A. LeBel, and T. Dickey (2012), An overview of sea state conditions and air-sea fluxes during RaDyO, *Journal of*

Geophysical Research – Oceans, 117(C00H19), doi:10.1029/2011JC007336. [Published, Refereed].

Zappa, C. J., M. L. Banner, H. Schultz, A. Corrada-Emmanuel, L. B. Wolff, and J. Yalcin (2008), Retrieval of short ocean wave slope using polarimetric imaging, *Measurement Science and Technology*, 19(055503), doi:10.1088/0957-0233/1019/1085/055503. [Published, Refereed].